Nanoscale

Predicting Plasma Conditions Necessary for Synthesis of γ-Al_2O_3 Nanocrystals

Journal:	*Nanoscale*
Manuscript ID	NR-ART-04-2021-002488.R1
Article Type:	Paper
Date Submitted by the Author:	02-Jun-2021
Complete List of Authors:	Cendejas, Austin; Washington University in Saint Louis, Energy, Environmental and Chemical Engineering Sun, He; Washington University, Chemistry Hayes, Sophia; Washington University, Chemistry Kortshagen, Uwe; Univ Minnesota Thimsen, Elijah; Washington University in Saint Louis, Energy, Environmental and Chemical Engineering

ARTICLE

Predicting Plasma Conditions Necessary for Synthesis of γ-Al_2O_3 Nanocrystals

Received 00th January 20xx,
Accepted 00th January 20xx

DOI: 10.1039/x0xx00000x

Austin J. Cendejas[1], He Sun[2,3], Sophia E. Hayes,[2,3], Uwe Kortshagen[4], Elijah Thimsen[1,3*]

Nonthermal plasma (NTP) offers a unique synthesis environment capable of producing nanocrystals of high melting point materials at relatively low gas temperatures. Despite the rapidly growing material library accessible through NTP synthesis, designing processes for new materials is predominantly empirically driven. Here, we report on the synthesis of both amorphous alumina and γ-Al_2O_3 nanocrystals and present a simple particle heating model that is suitable for predicting the plasma power necessary for crystallization. The heating model only requires the composition, temperature, and pressure of the background gas along with the reactor geometry to calculate the temperature of particles suspended in the plasma as a function of applied power. Complete crystallization of the nanoparticle population was observed when applied power was greater than the threshold where the calculated particle temperature is equal to the crystallization temperature of amorphous alumina.

Introduction

Nonthermal plasma (NTP) is a well-established means of synthesizing high-purity size controlled nanocrystals.[1] The unique nonequilibrium environment of NTP provides many advantages when compared to liquid-phase nanocrystal synthesis. For example, the unipolar negative charging of particles in the plasma prevents agglomeration without the need for surface ligation by long organic molecules.[1,2] Over the last two decades, the material library accessible by NTP has increased significantly. There has been much work surrounding the NTP synthesis of Group IV semiconductor nanocrystals[3–8] and their alloys,[9–11] as well as transparent conductive oxides.[12–17] More recently, NTP synthesis has been extended to include Group III-V semiconductor nanocrystals[18–20] and ceramic nanocrystals.[21–25] However, despite the rapidly growing material library accessible via NTP, there lacks a straightforward approach to designing synthesis processes for unexplored materials. For example, the ability to predict synthesis conditions (i.e. reactor geometry, gas composition, pressure, and power) that avoid amorphous material and instead yield crystalline nanoparticles would aid greatly in designing new synthesis techniques; and perhaps more crucially, would drastically reduce the amount of trial and error necessary in order to realize a new material via NTP.

One significant advantage of NTP compared to other gas-phase synthesis methods (e.g. flames) is the ability to synthesize crystalline materials at gas temperatures significantly lower than the temperature required for crystallization.[1,26] It is known that nanoparticles suspended in the plasma are selectively heated, often to several hundreds of Kelvin higher than the surrounding gas. Several groups have investigated the particle heating and cooling mechanisms in NTP both numerically[27,28] and experimentally.[29–32] The primary source of particle heating in NTP has been shown to be ion-electron recombination on the particle surface, while the primary cooling mechanism is conduction to the surrounding gas.[29] Additionally, particles undergo large temperature spikes on the 100 microsecond timescale due to the stochastic nature of recombination events; however, the magnitude of these spikes decreases with increasing particle diameter.[27] Despite the size-dependence of the transient fluctuations, it has been shown that particle temperature reaches an average value that is higher than the background gas and nominally independent of size.[27]

Kramer et al. have demonstrated that for Si nanocrystals, when the plasma conditions are such that the average particle temperature exceeds the crystallization temperature, the entire population of particles is crystalline.[30] In order to design a NTP synthesis reactor, it is therefore desirable to be able to predict the synthesis conditions under which the particle temperature will exceed this threshold and nanocrystals will be formed. Previous studies suggest that power delivered to the plasma and total pressure in the plasma are two key tuneable process parameters that significantly impact particle temperature, with increasing power and decreasing pressure leading to an increase in particle temperature.[30,33,34] These trends can be understood in terms of the heating and cooling mechanisms: an increase in plasma density with increased power causes increased particle heating through larger rates of exothermic surface reactions such as electron-ion recombination, and a decrease in conductive cooling rate with decreasing pressure. While monitoring and controlling pressure is straightforward in low pressure NTP systems, conventional

1. *Department of Energy, Environmental and Chemical Engineering, Washington University in Saint Louis, Saint Louis, Missouri*
2. *Department of Chemistry, Washington University in Saint Louis, Saint Louis, Missouri*
3. *Institute of Materials Science and Engineering, Washington University in Saint Louis, Saint Louis, Missouri*
4. *Department of Mechanical Engineering, University of Minnesota, Minneapolis, Minnesota*

means of measuring the plasma density (i.e. Langmuir probes) are nontrivial in dusty plasmas.[35] From this perspective, the capability to predict average particle temperature using only external, tuneable process parameters would be useful for designing synthesis approaches to further extend the material library accessible via NTP.

In this work, we present a simple nanoparticle heating model that can be used to predict the threshold plasma power necessary for NTP synthesis of nanocrystals. The model requires only four inputs: the pressure, temperature, and composition of the background gas, and plasma volume to determine particle temperature as a function of applied power. Given the unique potential of NTP to yield nanocrystals of very high melting point materials at low background temperature, Al_2O_3 was chosen as a target material. Al_2O_3 has a reported crystallization temperature between 1100-1300 K.[24,36,37] The crystallinity of Al_2O_3 nanoparticles was used as a probe for the particle temperature while suspended in the plasma. In this approach, the entire population of particles is expected to become crystalline when the average particle temperature exceeds the crystallization temperature (see Figure 1).

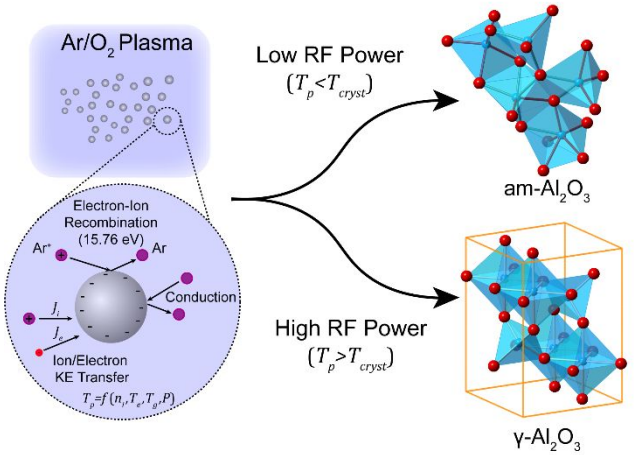

Figure 1. Conceptual schematic of energy transfer mechanisms in the plasma that lead to particle heating which can exceed the crystallization temperature when a threshold radiofrequency (RF) power is reached. Amorphous alumina (am-Al_2O_3).

Experimental Methods

Al_2O_3 Nanocrystal Synthesis.

Al_2O_3 nanocrystals were synthesized in a flow-through tubular nonequilibrium plasma reactor similar to one recently described by our group.[38] A detailed schematic of the experimental setup can be seen in Figure 2. In brief, the Al_2O_3 nanocrystals were synthesized in an Ar/O_2 plasma maintained in a fused-quartz tube with inner and outer diameters of 20 and 25 mm, respectively. Trimethylaluminium (TMA, Strem, Newburyport, MA) served as the aluminium precursor and was introduced into the reactor via a gas bubbler maintained at 225 Torr and swept by 20 standard cubic centimetres per minute (SCCM) Ar (Praxair, UHP 5.0). The resulting TMA feed rate was calculated to be 1.1 SCCM. Just upstream of the plasma zone, an additional stream containing 120 SCCM Ar and 10 SCCM O_2 (Praxair, UHP 5.0) was co-fed with the diluted TMA stream into the plasma. All flow rates were regulated using mass flow controllers (Type 1159, MKS Instruments, Andover, MA). The plasma was maintained via capacitively coupled radiofrequency power (RF, 13.56 MHz) applied to two stainless-steel ring electrodes, with the upstream electrode being powered and the downstream serving as the ground. The electrodes had inner and outer diameter of 25.4 mm and 38.1 mm, respectively, with a thickness of 15.9 mm and were separated by 30 mm. The input power was maintained at the setpoint using a 13.56 MHz RF power supply (AG0613, T&C Power Conversion, Rochester, NY) and impedance matching network (AIT600, T&C Power Conversion, Rochester, NY). All values for plasma power reported are the setpoint power as indicated on the RF power supply. The pressure during synthesis was measured immediately downstream of the plasma zone by a capacitance manometer (DMA Baratron, MKS Instruments, Andover, MA). Background gas temperatures, T_{gas}, were estimated by thermal imaging (SEEK Thermal Compact LW-AAA, Santa Barbara, CA) of the plasma reactor during discharge (see Supplementary Information for details) as previously reported.[34] The background gas temperature was taken as the value at the midpoint between the two ring electrodes.

The as-synthesized aerosol stream was diverted from the bypass line into a collection path where powder was collected on removable stainless steel 400 mesh filters or lacey carbon transmission electron microscopy (TEM) grids (part number 01824, Ted Pella, Redding CA). During powder collection on stainless steel filters, a diaphragm valve immediately before the rotary vane vacuum pump was adjusted to maintain the pressure in the plasma zone at 7.1 Torr. Stainless steel filters were weighed before and after powder collection to calculate mass production rates, which were between 125-250 mg/hr.

Post treatment annealing of alumina nanoparticles was carried out using a tube furnace (Linberg Blue M, ThermoFisher Scientific, Waltham, MA) under 500 SCCM Ar flow. The crucible (CoorsTek, Golden CO) was 1.5×1×7 cm in size and comprised of grade AD-998 alumina (min. 99.8% pure). The furnace tube was evacuated after sample loading and subsequently backfilled with Ar, this process was repeated two times followed by a 15 minute period of purging with Ar before the furnace was turned on. The ramp rate during heating of the tube furnace was approximately 2.5 K per minute. After annealing, the samples cooled down to room temperature over several hours while remaining under the inert atmosphere.

Electron Microscopy.

All images of the particles and selected-area electron diffraction (SAED) patterns were collected using a thermal emission transmission electron microscope (TEM) equipped with a LaB_6 filament (JEOL JEM-2000 FX) operated at an accelerating voltage of 200 kV. Particle size distributions were obtained using the ImageJ software package by fitting an ellipsoid around the particle and calculating the diameter of a circle with the same area. A minimum of 150 particles were counted for every size distribution and the subsequent histograms were fit with a

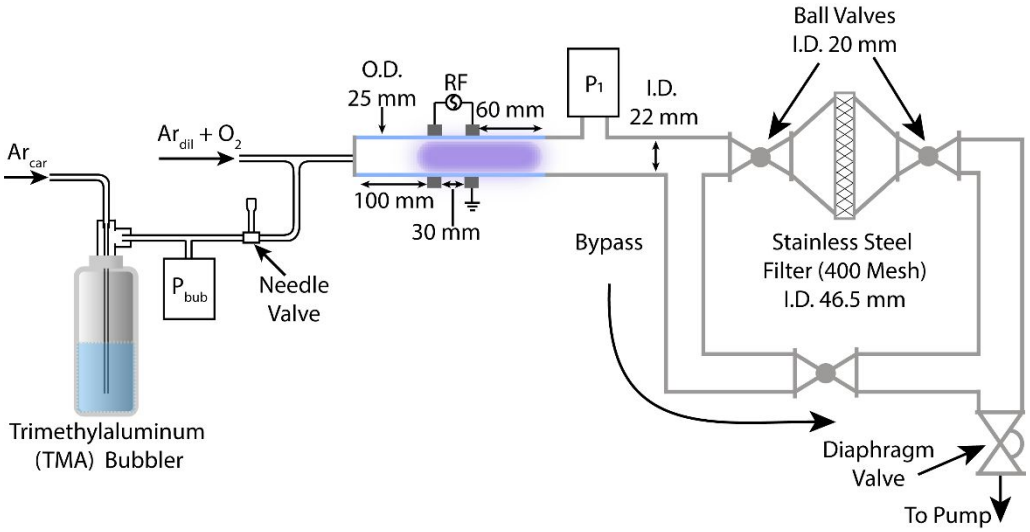

Figure 2. Schematic of the NTP apparatus used to synthesize alumina nanoparticles.

lognormal distribution to calculate mean diameter and geometric standard deviation.

X-Ray Diffraction.

After powder collection, a sample of the powder was taken from the stainless-steel filter and characterized by x-ray diffraction (XRD) to determine the crystal structure of the powder. Approximately 5 mg of dry powder was packed on a miscut Si wafer (MTI Corporation, Richmond, CA) with low-background signal and spectra were acquired using a d8 Advance diffractometer (Bruker, Billerica, MA) equipped with a Cu radiation source (Cu Kα, λ = 1.541 Å). All XRD patterns were collected for 2ϑ values in the range 20-80 degrees, with a step size of 0.02 degrees and a dwell time of 0.5 seconds per step.

Solid State NMR.

For ^{27}Al solid-state NMR (SSNMR) measurements, approximately 75 mg of dry powder of each sample was collected for analysis. The powder was packed into zirconia rotors (with low-aluminum background). NMR experiments were executed on a 14 Tesla instrument,^{27}Al Larmor frequency of 156.00 MHz, at magic-angle spinning (MAS) rotational frequencies of 35 kHz. A Bloch decay sequence with a short tip angle pulse (π/18)[39] was used with typical pulse lengths of 0.2 μs, collecting 8k transients, and using a recycle delay of 0.1 s. Samples were referenced to γ-Al_2O_3 as a secondary reference. Spectra were deconvoluted using the Dmfit program,[40] employing both the Czjzek model as well as an analysis of spinning sidebands (from quadrupolar satellites) that underlie the central transition resonances.

Results and Discussion

Nanoparticle temperature while suspended in NTP can be calculated by performing an energy balance on the particle using the heating and cooling mechanisms in the plasma. Specifically, the ion-electron recombination rate and the conduction to the background gas are the two dominant mechanisms for nanoparticles in which melting is not occurring. The particle energy balance as described by Mangolini and Kortshagen can be written as[27]

$$\frac{4}{3}\pi r_p^3 \rho C \frac{dT_p}{dt} = G - L \qquad (1)$$

where ρ is the material density, *C* is the specific heat, r_p is the particle radius, and T_p is the particle temperature. The terms *G* and *L* are the heat generation and heat sink terms, respectively. The heat generation term, *G*, is considered as the energy deposited to the particle at the surface through ion-electron recombination events. We are here neglecting additional energy release through surface chemical reactions, as these are poorly known. We can rationalize this choice by assuming that most of the chemical precursors have already been consumed by the formation of the particles. The rate of energy deposition through electron-ion recombination can be calculated as $G = J_{ion}\Delta H_{ion}$, where J_{ion} is the ion flux to the particle surface and ΔH_{ion} is the ionization energy of Ar, which is 15.76 eV. The ion flux is calculated by assuming the particles collect ions with the orbital motion limited (OML) current.[41] The resulting heat generation term is thus,

$$G = \frac{\Delta H_{ion}}{4} S_p n_i \sqrt{\frac{8k_B T_i}{\pi m_i}} \left(1 - \frac{e\Phi_p}{k_B T_i}\right) \qquad (2)$$

where S_p is the particle surface area and n_i, T_i, and m_i are positive ion density, temperature, and mass, respectively. The particle surface potential is denoted Φ_p and can be found by equating the positive ion and electron currents at the particle surface. The particle potential was found to be $\Phi_p = -4.5 k_B T_e / e$, which is a reasonable value for a nonequilibrium argon plasma. The ions were considered to have the same temperature as the background gas, T_{gas}, and only singly charged positive ions were considered. The heat sink term due to conduction, L, can be calculated in the same way previously reported[27] as,

$$L = \frac{1}{4}\eta_{Kn} n_{gas} S_p \sqrt{\frac{8k_B T_{gas}}{\pi m_{gas}}} \times \frac{3}{2} k_B \left(T_p - T_{gas}\right) \quad (3)$$

where n_{gas} is the total background gas density, m_{gas} is the atomic mass of the background gas, and η_{Kn} is the Knudsen accommodation coefficient which is expected to have a value between 0.1-1.[42]

By equating the heat generation and sink terms, a steady state temperature can be calculated. This temperature can be thought of as the average temperature a particle experiences while suspended in the plasma. The fluctuations from this average particle temperature are relatively small for particles larger than 10 nm in diameter, which is the case in the present work.[27,28] The average particle temperature can thus be calculated for an argon plasma as

$$T_p = T_{gas} + \frac{2T_{gas} n_i \Delta H_{rec}}{3\eta_{Kn} P}\left(1 - \frac{e\Phi_p}{k_B T_{gas}}\right) \quad (4)$$

where n_i is the ion density and P is the total pressure. We call the second term on the right-hand side, the "excess particle temperature", defined as the difference between the particle and the background gas temperature. Thus, particle temperature in NTP depends on four key parameters: ion density, electron temperature, background gas temperature, and pressure. Both pressure and background gas temperature can be measured in straightforward ways, but the ion density and electron temperature typically require complex plasma diagnostic techniques. However, typical methods of measuring the plasma density such as Langmuir probes and optical emission spectroscopy are often not suitable for dusty plasmas or when complex gas mixtures often used in synthesis processes are employed.[35]

To avoid the need for complex plasma diagnostics entirely, the ion density is estimated by considering the collision frequency of electrons in the discharge to determine the average power absorbed per electron. First, the electron energy distribution function (EEDF) must be obtained. A Boltzmann solver[43,44] was used to determine the electric field where ionization balances electron losses by ambipolar diffusion for the background gas composition and pressure used in this work. Given the EEDF (Supplementary Figure S1), the associated energy loss due to collisions can be calculated as the product of the collision frequency and the threshold energy of each inelastic collision. The average electron is thus found to absorb $\theta = 1.17 \times 10^8$ eV/s. The electron density can then be calculated as,

$$n_e = \frac{P_{abs}}{e\theta V} = \frac{\eta_{pwr} P_{set}}{e\theta V} \quad (5)$$

where P_{abs} is the power absorbed by the discharge and V is the plasma volume. The absorbed power is defined as the product of the setpoint power and the efficiency of the power delivery, η_{pwr}. Previous characterization of the power delivery in a similar reactor using the same power supply and matching network revealed the power delivery to be approximately 65% efficient.[34] Using the glow visible to the naked eye during synthesis, the plasma volume was determined to be approximately 60 cm^3. The synthesis apparatus is illustrated in Figure 2, and the details can be found in the experimental methods section. The result is an expression that can be used to calculate the electron density as a function of power, which is assumed equal to the positive ion density. If Eq. 5 is substituted into Eq. 4 for n_i, then the excess temperature has a factor η_{pwr} / η_{Kn}. These efficiencies are system specific. In our system, the ratio is assumed to be unity and experimental agreement was found with particle temperatures calculated using the setpoint power (*vide infra*). The assumption of positive ion density equal to electron density is justified by the feed gas being greater than 90% argon. In addition to the ion density, the EEDF can be used to determine the electron temperature, T_e, which is taken as 2/3 of the mean electron energy.[34] Finally, the background gas temperature was estimated by infrared imaging of the reactor walls during operation. A previous study by our group in a similar reactor compared the wall temperature measured by infrared imaging to the centreline temperature measured by a fibre optic fluorescence decay probe.[34] In Figure 3, the wall temperature measured by infrared imaging is taken as the lower bound of T_{gas}, while the upper bound is calculated by adding the fractional error reported in our previous work as a function of wall temperature. The average particle temperature of 10 nm diameter Al_2O_3 nanoparticles, which is the experimentally measured size in this work (*vide infra*), is presented as a function of absorbed power in Figure 3. Nanoparticle synthesis at conditions at which the calculated particle temperature is above the crystallization temperature are expected to result in the synthesis of an entirely crystalline

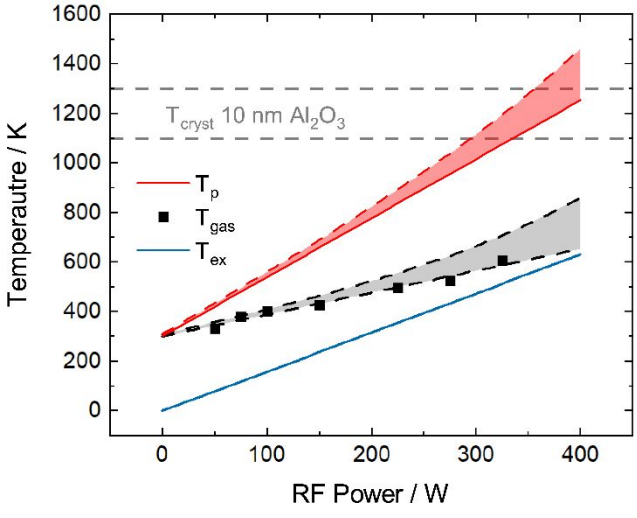

Figure 3. Particle temperature for 10 nm Al_2O_3 nanoparticles as a function of applied power (red). The particle temperature is the sum of the excess particle temperature (blue) and the linear fit (black dashed line) to the background gas temperature measurements (black squares). The shaded bands for background gas temperature and particle temperature account for the error associated with the use of the wall temperature to estimate the background gas temperature. The area bounded by gray dashed lines represents the reported values for crystallization temperatures of 10 nm Al_2O_3 nanostructures.

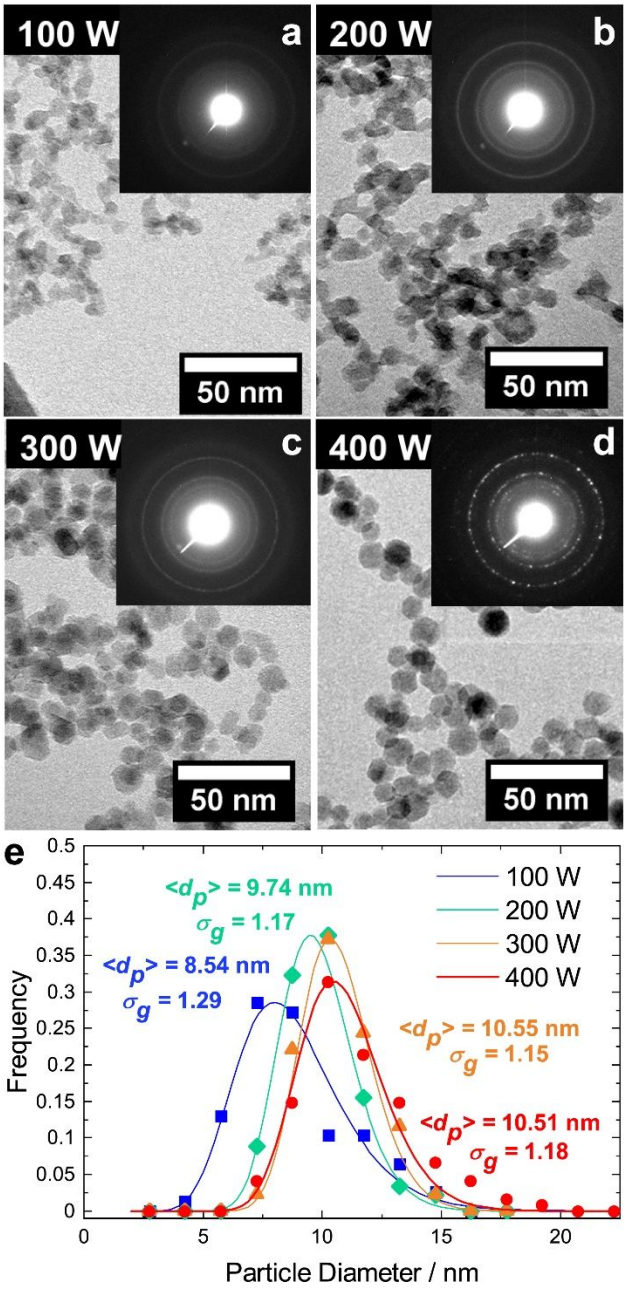

Figure 4. Transmission electron microscopy images and SAED patterns (a)-(d) of alumina nanoparticles synthesized at various powers. Size distributions (e) for alumina nanoparticles shown in (a)-(d), average particle diameter and geometric standard deviation of the lognormal fit is presented.

population of Al_2O_3 nanoparticles.

In Figure 3, complete crystallization is expected to occur when the power supplied to the plasma exceeds approximately 325 W. To test that prediction, experiments were conducted in which the RF power supplied to the plasma was adjusted from 100 W to 400 W. At all powers, spheroidal particles between 8-10 nm were synthesized as seen in Figure 4. The SAED patterns of nanoparticles synthesized at low power (Fig. 4a) revealed the particles to be amorphous while those synthesized at high power (Fig. 4d) exhibited an SAED pattern consistent with crystalline γ-Al_2O_3. The particle size did not significantly increase at higher synthesis powers (Fig. 4e). Thus, the higher particle temperature experienced during synthesis at elevated power did not lead to significant sintering, which is consistent with the expectation of suppressed aggregation in the plasma due to unipolar negative charging.[1,41]

To determine the crystallization temperature of the Al_2O_3 nanoparticles, post-synthesis annealing experiments were carried out. Samples containing amorphous alumina nanoparticles synthesized at 100 W were examined by XRD as seen in Figure 5. The as-deposited powder did not exhibit clear peaks in the XRD spectrum, consistent with the SAED pattern and thus confirming the powder was predominantly amorphous. As the annealing temperature was increased from 900 K to 1200 K, peaks consistent with the γ-Al_2O_3 crystal structure emerged. Based on the clear presence of the γ-Al_2O_3 peaks in the samples annealed above 1100 K, that temperature can be taken as the crystallization temperature of the Al_2O_3 nanoparticles synthesized in this study. A crystallization temperature of 1100 K is within the range of values reported for similar nanostructured Al_2O_3 in the literature.[24,36,37]

As a result of the particle heating in the nonthermal plasma, an increase in plasma synthesis power should eventually result in the crystallization of nanoparticles synthesized in the plasma. Alumina nanoparticles were synthesized at increasing powers between 100 W and 400 W at 50 W increments. The XRD patterns of these as-deposited powders can be seen in Figure 6. For samples synthesized at 150 W or higher, peaks corresponding to γ-Al_2O_3 can be seen. Additionally, the peaks become more intense with increasing power between 150 W and 300 W, indicating that the crystalline fraction of the powder sample is increasing. At synthesis powers above 300 W, the XRD patterns remain unchanged, indicating that complete crystallization of the nanoparticles occurred at 300 W. The calculated particle temperature at 300 W is 1050 K, which is in good agreement with the crystallization temperature determined by the thermal annealing experiments in Figure 5. Interestingly, for the nanoparticles synthesized at powers between 150 W and 300 W, the samples clearly show the presence of diffraction peaks, indicating that a portion of the population is crystalline, which is unexpected given the calculated average particle temperatures and the results from the thermal annealing experiment. This discrepancy can be explained in one of two ways. First, the nanoparticle heating model described here is an obvious simplification of all the heating and cooling mechanisms occurring during nanoparticle synthesis in a low-temperature plasma. Specifically, it has been shown that surface reactions can have a significant impact on the heating of relatively large particles (i.e. particles greater than 5 nm in diameter) in the Si/H system.[30] However, a recent report on Al_2O_3 atomic layer deposition on Y_2O_3-stabilized ZrO_2 nanoparticles found that temperature excursions due to the formation of Al_2O_3 on the surface are only on the order of 10s of Kelvin for nanoparticles of a similar diameter, suggesting the contribution from surface reactions may be less significant in the Al/O system.[45] Second, the particles in this process are growing while being heated and the growth mechanism is not completely understood.

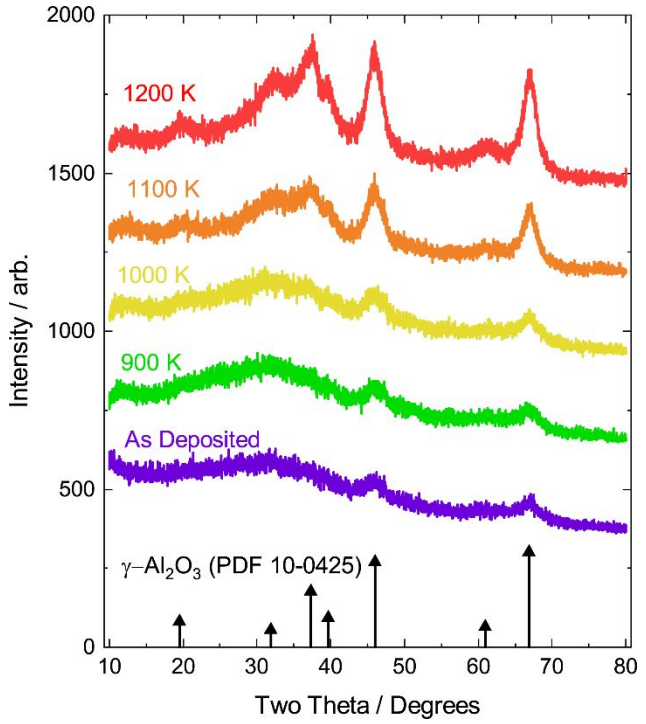

Figure 5. XRD spectra of Al_2O_3 nanoparticles synthesized at 100 W both as-deposited and after annealing at the indicated temperature for 3 hours. Pattern for γ-Al_2O_3 (PDF 10-0425) shown for reference.

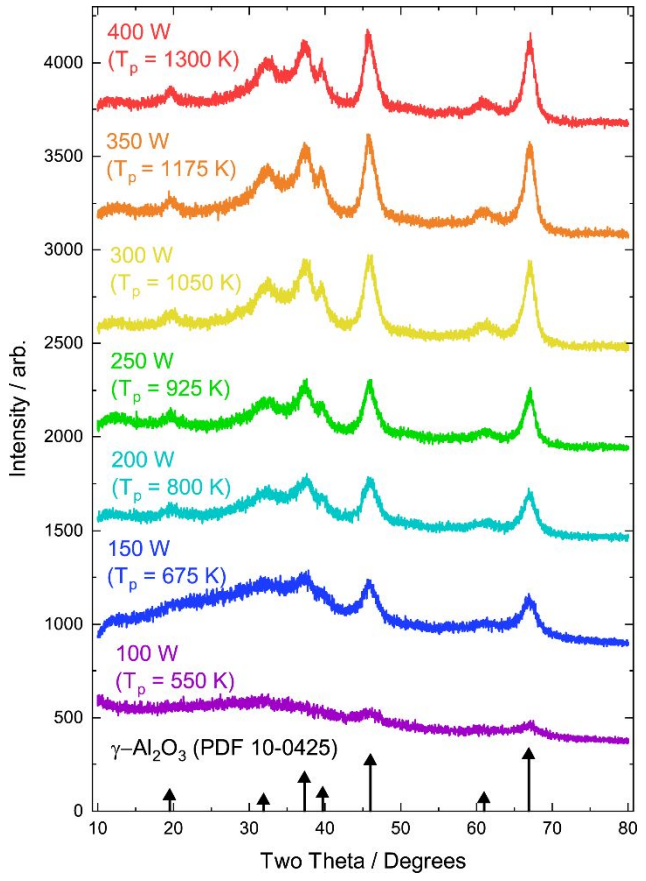

Figure 6. XRD spectra for alumina nanoparticles synthesized at various RF powers. The particle temperature calculated by Eq. 4 corresponding to each synthesis power is in parentheses.

As a result, it is possible that the particles experience large excursions from the average particle temperature as they are growing and could become partially crystallized before growing to a point at which the average particle temperature is less than the crystallization temperature. Regardless, the power required to fully crystallize the population agrees well with the predicted particle temperature; and lesser applied powers appear to result in some amorphous fraction in the powder.

To characterize the amorphous fraction of the alumina nanoparticles as a function of the synthesis power, ^{27}Al SSNMR experiments were carried out (under MAS) to determine the local coordination environment of the aluminium cations in the nanoparticles. The SSNMR spectra (showing just the central transitions) of samples prepared between 100 W and 400 W can be seen in Figure 7. In the case of alumina nanoparticles synthesized at 100 W, three peaks are present, appearing at approximately 2, 30, and 60 ppm corresponding to $^{[VI]}$Al, $^{[V]}$Al, and $^{[IV]}$Al species, respectively. Fitting of these peaks yielded the expected isotropic chemical shifts for the respective aluminium coordination numbers (supporting information). The presence of $^{[V]}$Al is an indication the sample has an amorphous structure.[46–48] At 200 W, the $^{[V]}$Al peak diminishes almost entirely consistent with crystalline phases of Al_2O_3, with a small presence of an amorphous fraction, in agreement with the XRD analysis. At powers of 300 W and 400 W, the SSNMR patterns are similar and contain only 4- and 6-coordinate aluminium cations, consistent with the crystal structure of γ-Al_2O_3.[48,49] The SSNMR peaks were fit using the Czjzek model,[50–52] in a similar method to previous studies on amorphous and γ-Al_2O_3 (see Supporting Information).[40] The ratio of tetrahedral to octahedral aluminium sites is found to be similar for all samples. The disappearance of the 5-coordinate $^{[V]}$Al resonance at 300 W and 400 W further supports the conclusion that the particles become crystallized in the γ phase at powers 300 W or greater.

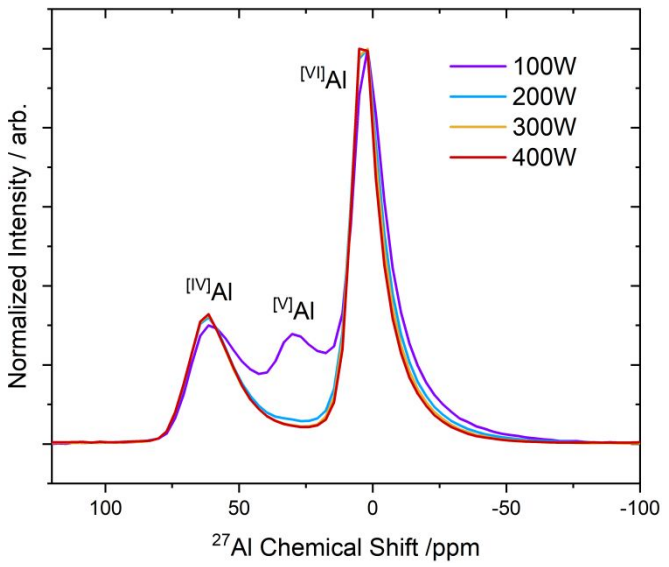

Figure 7. ^{27}Al MAS solid-state NMR spectra at 14 T of the central transitions of as-synthesized alumina nanoparticles synthesized at various applied RF power. The MAS rotational frequency (ν_R) is 35 kHz. The data have been normalized to the highest intensity peak.

Taken together with the XRD patterns in Figure 6, the results indicate the absence of other crystallographic phases of alumina such as: δ-, θ- and α-Al_2O_3 in these samples.

Conclusions

In this work, we developed an approach to predict NTP synthesis conditions that yield crystalline nanoparticles. We propose a simple particle heating model that yields an average particle temperature experienced in the NTP as a function of applied power. The model is unique in that it requires no complex plasma diagnostics for the inputs, but only depends on the reactor geometry, background gas temperature, pressure, and gas composition. The synthesis of Al_2O_3 nanoparticles was carried out to study the applicability of the model to a high crystallization temperature material. Specifically, the concept was demonstrated that there is a threshold power at which the particle temperature is equal to the crystallization temperature, above which the entire population of particles becomes crystalline. Solid-state NMR of ^{27}Al helped establish the aluminium cation coordination environments, in non-crystalline samples (prepared at lower RF power), when XRD was unable to lend structural insights. The Al_2O_3 nanoparticles were found to become increasingly crystalline with increases in power up to 300 W, at which point further increases in power did not have a significant effect on the crystalline fraction of the ensemble. This result is consistent with the idea of a threshold power for crystallization and was in good agreement with the predicted value of approximately 325 W from the particle heating model. This work provides a framework for designing NTP synthesis processes for high crystallization temperature materials by predicting conditions necessary to reach particle temperatures sufficient for nanocrystal formation.

Conflicts of interest

There are no conflicts to declare.

Author Contributions

A.J.C. performed nanocrystal synthesis and characterization under the supervision of E.T.; H.S. and S.E.H. performed solid state nuclear magnetic resonance spectroscopy experiments and analysed the data; U.K. performed Boltzmann solver calculations of the EEDF and nanoparticle excess temperature estimations; A.J.C. drafted the manuscript with E.T. using intellectual contributions from all authors. All authors discussed the contents of the manuscript.

Acknowledgements

The authors acknowledge financial support from the Army Research Office MURI grant W911NF-18-1-0240. This work was performed in part at the Institute of Materials Science and Engineering at Washington University in Saint Louis, and the authors acknowledge financial support for the use of instruments and staff assistance. This study made use of the National Magnetic Resonance Facility at Madison, which is supported by NIH grant P41GM136463, P41GM103399 (NIGMS), former number: P41RR002301. Equipment was purchased with funds from the University of Wisconsin-Madison, the NIH P41GM103399, S10RR02781, S10RR08438, S10RR023438, S10RR025062, S10RR029220), the NSF (DMB-8415048, OIA-9977486, BIR-9214394), and the USDA. H.S. acknowledges support from NSF award 1640899.

References

1 U. R. Kortshagen, R. M. Sankaran, R. N. Pereira, S. L. Girshick, J. J. Wu and E. S. Aydil, *Chem. Rev.*, 2016, **116**, 11061–11127.
2 M. V. Kovalenko, L. Manna, A. Cabot, Z. Hens, D. V. Talapin, C. R. Kagan, V. I. Klimov, A. L. Rogach, P. Reiss, D. J. Milliron, P. Guyot-Sionnnest, G. Konstantatos, W. J. Parak, T. Hyeon, B. A. Korgel, C. B. Murray and W. Heiss, *ACS Nano*, 2015, **9**, 1012–1057.
3 A. Bapat, C. Anderson, C. R. Perrey, C. B. Carter, S. A. Campbell and U. Kortshagen, *Plasma Phys. Control. Fusion*, 2004, **46**, B97–B109.
4 L. Mangolini, E. Thimsen and U. Kortshagen, *Nano Lett.*, 2005, **5**, 655–659.
5 R. Limpens, G. F. Pach and N. R. Neale, *Chem. Mater.*, 2019, **31**, 4426–4435.
6 R. Gresback, Z. Holman and U. Kortshagen, *Appl. Phys. Lett.*, 2007, **91**, 093119.
7 K. I. Hunter, N. Bedford, K. Schramke and U. R. Kortshagen, *Nano Lett.*, 2020, **20**, 852–859.
8 M. Macias-Montero, S. Askari, S. Mitra, C. Rocks, C. Ni, V. Svrcek, P. A. Connor, P. Maguire, J. T. S. Irvine and D. Mariotti, *Nanoscale*, 2016, **8**, 6623–6628.
9 X. D. Pi and U. Kortshagen, *Nanotechnology*, 2009, **20**, 295602.
10 O. Yasar-Inceoglu and L. Mangolini, *Materials Letters*, 2013, **101**, 76–79.
11 D. J. Rowe and U. R. Kortshagen, *APL Materials*, 2014, **2**, 022104.
12 P. Felbier, J. Yang, J. Theis, R. W. Liptak, A. Wagner, A. Lorke, G. Bacher and U. Kortshagen, *Advanced Functional Materials*, 2014, **24**, 1988–1993.
13 E. Thimsen, M. Johnson, X. Zhang, A. J. Wagner, K. A. Mkhoyan, U. R. Kortshagen and E. S. Aydil, *Nat Commun*, 2014, **5**, 5822.
14 B. L. Greenberg, S. Ganguly, J. T. Held, N. J. Kramer, K. A. Mkhoyan, E. S. Aydil and U. R. Kortshagen, *Nano Lett.*, 2015, **15**, 8162–8169.
15 B. L. Greenberg, Z. L. Robinson, K. V. Reich, C. Gorynski, B. N. Voigt, L. F. Francis, B. I. Shklovskii, E. S. Aydil and U. R. Kortshagen, *Nano Lett.*, 2017, **17**, 4634–4642.
16 Q. Chen and E. Thimsen, *ACS Appl. Mater. Interfaces*, 2020, **12**, 25168–25177.
17 B. Graves, S. Engelke, C. Jo, H. G. Baldovi, J. de la Verpilliere, M. D. Volder and A. Boies, *Nanoscale*, 2020, **12**, 5196–5208.
18 N. B. Uner, D. M. Niedzwiedzki and E. Thimsen, *J. Phys. Chem. C*, 2019, **123**, 30613–30622.
19 N. B. Uner and E. Thimsen, *J. Phys. D: Appl. Phys.*, 2020, **53**, 095201.
20 N. B. Uner and E. Thimsen, *Plasma Processes and Polymers*, 2020, **17**, 1900233.
21 D. Coleman, T. Lopez, O. Yasar-Inceoglu and L. Mangolini, *Journal of Applied Physics*, 2015, **117**, 193301.

22 A. Alvarez Barragan, N. V. Ilawe, L. Zhong, B. M. Wong and L. Mangolini, *J. Phys. Chem. C*, 2017, **121**, 2316–2322.
23 D. Coleman and L. Mangolini, *ACS Omega*, 2019, **4**, 10089–10093.
24 Z. Li, P. R. Wray, M. P. Su, Q. Tu, H. P. Andaraarachchi, Y. J. Jeong, H. A. Atwater and U. R. Kortshagen, *ACS Omega*, 2020, **5**, 24754–24761.
25 S. Askari, A. U. Haq, M. Macias-Montero, I. Levchenko, F. Yu, W. Zhou, K. (Ken) Ostrikov, P. Maguire, V. Svrcek and D. Mariotti, *Nanoscale*, 2016, **8**, 17141–17149.
26 T. Lopez and L. Mangolini, *Nanoscale*, 2014, **6**, 1286–1294.
27 L. Mangolini and U. Kortshagen, *Phys. Rev. E*, 2009, **79**, 026405.
28 N. B. Uner and E. Thimsen, *J. Phys. Chem. C*, 2017, **121**, 12936–12944.
29 H. R. Maurer and H. Kersten, *J. Phys. D: Appl. Phys.*, 2011, **44**, 174029.
30 N. J. Kramer, R. J. Anthony, M. Mamunuru, E. S. Aydil and U. R. Kortshagen, *J. Phys. D: Appl. Phys.*, 2014, **47**, 075202.
31 T. Lopez and L. Mangolini, *Journal of Vacuum Science & Technology B*, 2014, **32**, 061802.
32 B. Alessi, M. Macias-Montero, C. Maddi, P. Maguire, V. Svrcek and D. Mariotti, *Faraday Discuss.*, 2020, **222**, 390–404.
33 N. J. Kramer, E. S. Aydil and U. R. Kortshagen, *J. Phys. D: Appl. Phys.*, 2015, **48**, 035205.
34 N. B. Uner and E. Thimsen, *Plasma Sources Sci. Technol.*, 2018, **27**, 074005.
35 L. Mangolini, *J. Phys. D: Appl. Phys.*, 2017, **50**, 373003.
36 S. K. Lee and S. Ryu, *J. Phys. Chem. Lett.*, 2018, **9**, 150–156.
37 A. Mavrič, M. Valant, C. Cui and Z. M. Wang, *Journal of Non-Crystalline Solids*, 2019, **521**, 119493.
38 A. Cendejas, D. Moher and E. Thimsen, *Journal of Vacuum Science & Technology A*, 2020, **39**, 012406.
39 E. Lippmaa, A. Samoson and M. Magi, *J. Am. Chem. Soc.*, 1986, **108**, 1730–1735.
40 D. Massiot, F. Fayon, M. Capron, I. King, S. L. Calvé, B. Alonso, J.-O. Durand, B. Bujoli, Z. Gan and G. Hoatson, *Magnetic Resonance in Chemistry*, 2002, **40**, 70–76.
41 U. Kortshagen and U. Bhandarkar, *Phys. Rev. E*, 1999, **60**, 887–898.
42 J. E. Daugherty and D. B. Graves, *Journal of Vacuum Science & Technology A*, 1993, **11**, 1126–1131.
43 T. M. York, *Appl Opt*, 1981, **20**, 1360.
44 U. Kortshagen, H. Schluter and A. Shivarova, *J. Phys. D: Appl. Phys.*, 1991, **24**, 1571–1584.
45 B. L. Greenberg, K. P. Anderson, M. A. Wolak, A. G. Jacobs, J. A. Wollmershauser and B. N. Feigelson, *Chem. Mater.*, , DOI:10.1021/acs.chemmater.0c03644.
46 S. K. Lee, S. Y. Park, Y. S. Yi and J. Moon, *J. Phys. Chem. C*, 2010, **114**, 13890–13894.
47 J. Cui, M. G. Kast, B. A. Hammann, Y. Afriyie, K. N. Woods, P. N. Plassmeyer, C. K. Perkins, Z. L. Ma, D. A. Keszler, C. J. Page, S. W. Boettcher and S. E. Hayes, *Chem. Mater.*, 2018, **30**, 7456–7463.
48 C. V. Chandran, C. E. A. Kirschhock, S. Radhakrishnan, F. Taulelle, J. A. Martens and E. Breynaert, *Chem. Soc. Rev.*, 2019, **48**, 134–156.
49 L. Samain, A. Jaworski, M. Edén, D. M. Ladd, D.-K. Seo, F. Javier Garcia-Garcia and U. Häussermann, *Journal of Solid State Chemistry*, 2014, **217**, 1–8.
50 G. Czjzek, J. Fink, F. Götz, H. Schmidt, J. M. D. Coey, J.-P. Rebouillat and A. Liénard, *Phys. Rev. B*, 1981, **23**, 2513–2530.
51 J.-B. d'Espinose de Lacaillerie, C. Fretigny and D. Massiot, *Journal of Magnetic Resonance*, 2008, **192**, 244–251.
52 G. L. Caër, B. Bureau and D. Massiot, *J. Phys.: Condens. Matter*, 2010, **22**, 065402.